Endmember Extraction Using the Physics-Based Multi-Mixture Pixel Model

Ryan Close[a], Paul Gader[b], Alina Zare[c], Joseph Wilson[b], Dmitri Dranishnikov[b]

[a]U.S. Army RDECOM CERDEC NVESD, Ft. Belvoir, VA;

[b]Department of Computer and Information Science and Engineering, University of Florida, Gainesville, FL, USA;

[c]Department of Electrical and Computer Engineering, University of Missouri, Columbia, MO, USA

ABSTRACT

A method of incorporating the multi-mixture pixel model into hyperspectral endmember extraction is presented and discussed. A vast majority of hyperspectral endmember extraction methods rely on the linear mixture model to describe pixel spectra resulting from mixtures of endmembers. Methods exist to unmix hyperspectral pixels using nonlinear models, but rely on severely limiting assumptions or estimations of the nonlinearity. This paper will present a hyperspectral pixel endmember extraction method that utilizes the bidirectional reflectance distribution function to model microscopic mixtures. Using this model, along with the linear mixture model to incorporate macroscopic mixtures, this method is able to accurately unmix hyperspectral images composed of both macroscopic and microscopic mixtures. The mixtures are estimated directly from the hyperspectral data without the need for *a priori* knowledge of the mixture types. Results are presented using synthetic datasets, of multi-mixture pixels, to demonstrate the increased accuracy in unmixing using this new physics-based method over linear methods. In addition, results are presented using a well-known laboratory dataset.

Keywords: Hyperspectral image analysis, physics-based mixture models, reflectance spectroscopy, nonlinear unmixing, microscopic mixture, macroscopic mixture, multi-mixture pixel

Distribution A: Public Release Unlimited

1. INTRODUCTION

A common research problem in hyperspectral image (HSI) analysis is that of estimating endmembers from a given set of pixels, often referred to as endmember extraction.[1-16] Often endmembers are extracted simultaneously with estimating of their respective proportions, this is known as pixel unmixing.[1-17] A vast majority of approaches to this problem rely on a linear model to describe the mixing relationships between endmembers.[17] An example is the linear mixture model (LMM) shown in Equation (1), with the corresponding constraints in Equation (2), where M is the number of endmembers in the scene, ϵ_i is an error term, and e_k and p_{ik} are the endmembers and proportions, respectively, of a given pixel x_i.[1, 6] Reliance on the linear model is a result of the mathematical amenability of linear models and the prevalence of macroscopic mixtures, also known as areal or checkerboard mixtures. Macroscopic mixtures occur when two or more endmembers are discretely present within the instantaneous field of view of a given pixel. [17] This mixing is caused by the coarse spatial resolution of the hyperspectral sensor and does not represent a physical mixing of endmembers.

$$x_i = \sum_{k=1}^{M} e_k p_{ik} + \epsilon_i \tag{1}$$

$$\forall_{ik}\ p_{ik} \geq 0 \quad \forall_i \sum_{k=1}^{M} p_{ik} = 1 \tag{2}$$

Research, however, has shown that nonlinear mixtures are present in hyperspectral images and have a substantial effect on measured spectral reflectance signatures over a given image. [17-19] Recently the impact of nonlinear mixtures in HSIs has garnered much attention. [17-52] Keshava and Mustard describe the effects of nonlinear mixing by stating[17]:

In tests of linear versus nonlinear mixing on laboratory data, the fractions calculated may be in error by as much as 30% absolute. In addition, the linear model can cause considerable ambiguity and false fractions when used on nonlinear mixtures. Absorption bands and continua in nonlinear mixtures cannot be adequately fit with a linear model.

Microscopic mixtures, also called intimate mixtures, are known to be present in many hyperspectral images. [17, 40, 53-62] Unlike the macroscopic mixture, microscopic mixtures form non-linear mixtures of endmember spectra. [54-57, 61, 62] Consequently, the LMM has been shown inadequate for modeling this type of mixing in hyperspectral data. [17, 40, 53-62] While microscopic mixing does represent physical mixtures of endmembers, it is important to note that it is not a chemical reaction (i.e., the constituent endmember substances still exist).

Attempts to incorporate the nonlinearity of microscopic mixtures into the hyperspectral pixel unmixing problem have been largely black-box approaches and often assume a known set of endmembers, thereby ignoring the endmember extraction problem. Traditional methods of reproducing an unknown nonlinear function such as neural networks [33, 37-39] and kernel methods [41, 49, 59, 60, 63-65] have been used to estimate the latent nonlinear function in the system. Recent research has introduced manifolds to model the nonlinearity in hyperspectral data.[20, 22-28, 46-48, 51, 52, 66-81] Typically used in hyperspectral classification applications, endmember and proportion estimation has also been pursued with manifold based algorithms. [35, 36, 82] These methods all attempt to account for the nonlinearity with a generic machine learning model to approximate the mixture; however they do not explicitly model the underlying physics of the mixture.

Two commonly referenced physics-based techniques for microscopic mixture pixel unmixing are Mustard and Pieters's least squared error (LSE) unmixing of single-scattering albedo data[53] and Guilfoyle, et al. use of a radial basis function neural network (RBFNN)[33]. However, these methods of microscopic mixture pixel unmixing require the assumption that a data set contains only macroscopically mixed data or microscopically mixed data and assume an known set of endmembers. [33, 40, 53, 54, 83-85]

Recently, two methods for pixel unmixing were developed that allow for proportion estimation in the presence of both macroscopic and microscopic mixtures. The first is a physics-based kernel approach that approximates Hapke's reflectance model. [59, 60, 63] The second is the microscopic mixture iterated constrained endmembers (MICE) algorithm.[86] These two approaches, however, assume that a given HSI pixel is composed exclusively of a single mixture type (i.e. either macroscopically or microscopically mixed). This assumption is valid for some HSIs. However, the assumption is violated in HSIs that contain overlapping heterogeneous regions of different mixture types. In these scenes a pixel may be composed of a macroscopic mixture, a microscopic mixture, or a combination of the two mixture types. A second violation to this assumption occurs when one or more endmembers of a microscopic mixture clump together. These particles cause macroscopic mixing with the surrounding microscopic mixture. These observations led to a new HSI pixel model, the multi-mixture pixel (MMP).[87] The MMP characterizes a pixel as a macroscopic mixture of endmembers and a microscopic mixture, i.e., a mixture of mixtures. The MMP model's introducing publication, however, assumed that the endmembers where known *a priori*. Often this assumption is not valid. This paper will build upon the MMP model and the introduced method of estimating proportions by adding the ability to extract endmembers simultaneously.

The remainder of this paper is organized as follows. Section 2 gives a review of microscopic mixtures and the bidirectional reflectance distribution function (BRDF). Next, in Section 3 the MMP model and the associated MMP proportion estimation (MPE) algorithm is discussed. Section 4 will introduce the MMP endmember extraction (MEE) algorithm. Section 5 presents experimental results on both synthetic data sets and well-known sets of laboratory mineral mixtures, the RELAB data sets. Finally, in Section 6 conclusions and future research is discussed.

2. REVIEW OF MICROSCOPIC MIXTURES

Microscopic mixing occurs when particles of different endmembers are homogenously distributed within the instantaneous field of view of a given pixel. Light incident on this mixed surface is scattered.[56, 61] The close proximity of endmembers particles, occurring in a microscopic mixture, causes multi-scattering between particles with differing spectral properties. [17, 54] This multi-scattering between particles causes a nonlinear mixture in reflectance spectra. To accurately estimate endmembers and proportions within the context of microscopic mixture reflectance spectra, a model for reflectance is needed.

Reflectance is characterized by the collimation of the light source and the detector (or sensor). Because perfect collimation and perfect diffuseness do not exist, in reality all reflectances are biconical. [56, 61] However, on a clear, sunny

day, the sun can be reasonably approximated as a collimated source (i.e., directional). [56] An air or space borne sensor looking at the ground approximates a directional detector. [56] Therefore, under these basic remote sensing assumptions (including assuming minimal cloud cover), the BRDF is the appropriate model for hyperspectral image applications.

Hapke's BRDF has been validated through experimentation and is widely accepted as an accurate model. [33, 38, 40, 41, 53-63, 83-85] Hapke's reflectance coefficient BRDF is given by Equation (3), where c_i and c_e are the cosine of the angles of incidence and emergence, respectively, g is the phase angle, $P(g)$ is the phase function for particles, $B(g)$ is the backscatter function given by Equation (4), $H(\mu)$ is Hapke's approximation to Chandrasekhar's function for isotropic multi-scattering given by Equation (5), and w is the average single-scattering albedo given by Equation (6) with P_S and P_A being the power of the incident irradiance scattered and absorbed by the particle, respectively. [33, 53-56, 59-61, 63] To clarify terms, c_i and c_e are used for the cosine of the angles of incidence and emergence instead of the traditional μ_0 and μ. The phase angle and the angles of incidence and emergence describe the geometries of the light source and detector. Scattering properties of the surface are described by the $P(g)$ function. The backscatter function $B(g)$ models the opposition effect, as given by Equation (4) where B_0 describes the magnitude of the opposition effect and h depends on the interparticle spacing.

$$R = \frac{w}{4(c_i + c_e)}\{[1 + B(g)]P(g) + H(c_i)H(c_e) - 1\} \tag{3}$$

$$B(g) = \frac{B_0}{1 + \left(\frac{1}{h}\right)\tan\left(\frac{g}{2}\right)} \tag{4}$$

$$H(c_{[i,e]}) = \frac{1 + 2c_{[i,e]}}{\left(1 + 2c_{[i,e]}(1 - w_\lambda)^{1/2}\right)} \tag{5}$$

$$w = \frac{P_S}{P_S + P_A} \tag{6}$$

Under remote sensing assumptions, the angle of incidence is commonly 15^0 to 40^0 and the angle of emergence 0^0, under these conditions the phase angle is between 15^0 and 40^0. [53] Additionally, under remote sensing assumptions, these angles are assumed constant over a given collection. Mustard and Pieters demonstrated that at phase angles greater than 15^0 the $B(g)$ was negligible. [53] Additionally, under the assumption of isotropic scattering (all light is scattered equally in all directions) the phase function is defined to be $P(g) = 1$. [56, 61] Using these remote sensing assumptions and the consequential results for $B(g)$ and $P(g)$, a simplified reflectance coefficient function can be derived as shown in Equation (7) where the λ subscript is used to signify the wavelength dependence of the reflectance function. Also, w_λ was added as a parameter to Chandrasekhar's function to represent the single-scattering albedo as an input parameter to the function. As the reflectance coefficient function, under the described assumptions, is the only model for reflectance used in this research it will simply be referred to as the reflectance function. The resulting reflectance function can be seen plotted against single-scattering albedo in Figure 1.

$$R_\lambda = \frac{w_\lambda}{4(c_i + c_e)}H(c_i, w_\lambda)H(c_e, w_\lambda) \tag{7}$$

The reflectance of a microscopic mixture is described by the reflectance function (Equation (7)) and the average single-scattering albedo of the mixture, shown in Equation (8). [53, 54, 56] The average single-scattering albedo is a linear combination of endmember's single-scattering albedos where Ψ_k, q_k, and d_k are the mass fraction, single particle density, and average effective particle size for a given mixture component (i.e., endmember). [56]

$$w_\lambda = \frac{\sum_{k=1}^{M}(\Psi_k/q_k d_k)\,w_{k\lambda}}{\sum_{k=1}^{M}(\Psi_k/q_k d_k)} \tag{8}$$

The average single-scattering albedo can also be represented as a relative geometric cross-section (F_k) or endmember proportion (f_k), shown in Equation (9) for the kth component. [56] This representation is important, because often in remote sensing the particle density and particle size of endmembers is not known. Therefore, the particle density and particle size are assumed roughly equal for all endmembers. Under this assumption, the proportion of an endmember composing a mixed pixel's spectra (i.e., the relative geometric cross-section of the pixel composed of the endmember) is equal to its mass fraction.

$$F_k = f_k = \frac{(\Psi_k / q_k d_k)}{\sum_{k=1}^{M}(\Psi_k / q_k d_k)} \qquad (9)$$
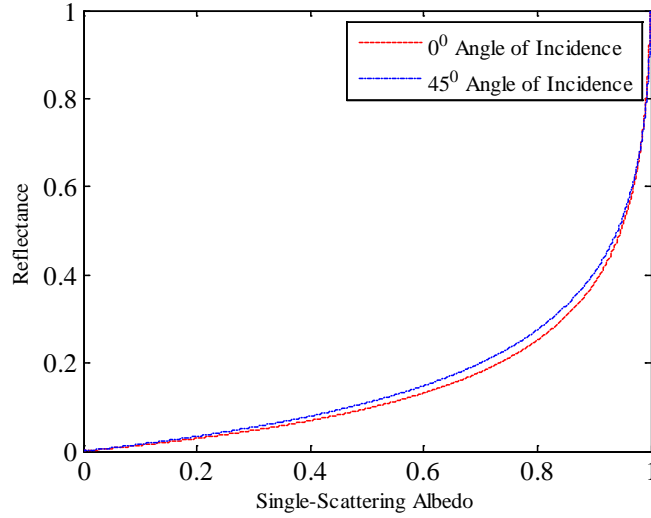

Figure 1: Reflectance function curve versus single-scattering albedo (angle of emergence is $\mathbf{0^0}$).

Using the relative geometric cross-section representation for each endmember, the equation for the average single-scattering albedo can be written as Equation (10). This formulation leads to constraints similar to those of the LMM: $f_k \geq 0$ and $\sum_{k=1}^{M} f_k = 1$. Additionally, the albedo-domain formulation given in Equation (10) can be represented in the reflectance-domain as shown by Equation (11), with the same constraints.

$$w_\lambda = \sum_{k=1}^{M} f_k w_{k\lambda} \qquad (10)$$

$$x_i = R\left(\sum_{k=1}^{M} f_{ik} w_k\right) \qquad (11)$$

3. MULTI-MIXTURE PIXELS

3.1 Multi-Mixture Pixel Model

The MMP model, shown in Equation (12), characterizes a pixel as a macroscopic mixture of endmembers and a microscopic mixture, i.e., a mixture of mixtures.

$$x_i = \sum_{k=1}^{M} p_{ik} e_k + p_{iM+1} R\left(\sum_{k=1}^{M} f_{ik} w_k\right) + \varepsilon_i \qquad (12)$$

The macroscopic proportions (p_{ik}) in the MMP model are dependent on the reflectance of the component microscopic mixture. Therefore, the macroscopic proportions are dependent on the microscopic proportions (f_{ik}). Estimation of the microscopic proportions is an ill-posed inversion problem. Ignoring noise, consider the following case, as illustrated in Figure 2. An MMP x is composed of two endmembers, e_1 and e_2. The MMP mixture point is constrained by the set of possible macroscopic mixtures between the endmembers, illustrated as a dashed blue line, and the set of possible microscopic mixtures between the endmembers, illustrated as a solid red curve. Recall that the MMP model treats the microscopic mixture as an endmember. Therefore, the MMP model can represent x with 0 residual error using e_1, e_2, and $r = R(\sum_{k=1}^{M} f_{ik} w_k)$ for any point r on the arc A. More precisely, $\forall r \in A \,\exists\, p_1, p_2, p_3 : x = p_1 e_1 + p_2 e_2 + p_3 r$.

As a pixel's microscopic mixture proportion (p_{iM+1}) increases, the MMP mixture point moves closer to the microscopic mixture line, as shown in Figure 3. Therefore, the plausible proportions of the microscopic mixture become increasingly constrained and even unique in the case of a 100% microscopic mixture, i.e., the arc A of plausible points r shrinks. As an MMP mixture point's microscopic mixture proportion lessens, the MMP mixture point moves closer to the

macroscopic mixture, as shown in Figure 4. This causes the plausible microscopic proportions to be less constrained, i.e., the arc A of plausible points r increases. However, as the microscopic mixture proportion decreases (i.e., the MMP is dominated by a macroscopic mixture) the microscopic mixture becomes less of a factor in the overall pixel's mixture proportions. Therefore, the error caused by the ill-posed inversion of estimating the microscopic proportions is a small factor in accurately estimating the mixture proportions.

3.2 MMP Proportion Estimation

Estimating proportions of the MMP model, termed MMP proportion estimation (MPE), is composed of two steps. First, the reflectance signature of the microscopic mixture component of the MMP must be estimated. To determine this reflectance signature, the microscopic mixture proportions are estimated using an albedo-domain microscopic mixture, given by Equation (13). This albedo-domain microscopic mixture term is derived from Equation (11), where $\boldsymbol{\beta_i}$ is an assumed zero-mean Gaussian additive noise term. . [1, 17, 53, 54, 59, 60, 63, 88] Estimation of the microscopic mixture proportions is accomplished by using quadratic programing to minimize the residual sum of squares (RSS) of Equation (13), as shown in Equation (14), with its associated constraints. Secondly, the macroscopic proportions are estimated by minimizing the RSS objective function shown in Equation (15), derived from the MMP model (Equation (12)). When estimating the macroscopic mixture proportions, the microscopic mixture proportions are held fixed.

$$R^{-1}(x_i) = \sum_{k=1}^{M} f_{ik} w_k + \beta_i \tag{13}$$

$$RSS = \sum_{i=1}^{N} \left(\left(R^{-1}(x_i) - \sum_{k=1}^{M} f_{ik} w_k \right)^T \left(R^{-1}(x_i) - \sum_{k=1}^{M} f_{ik} w_k \right) \right) \tag{14}$$

$$RSS = \sum_{i=1}^{N} \left(\left(x_i - \sum_{k=1}^{M} p_{ik} e_k - p_{iM+1} R\left(\sum_{k=1}^{M} f_{ik} w_k \right) \right)^T \left(x_i - \sum_{k=1}^{M} p_{ik} e_k - p_{iM+1} R\left(\sum_{k=1}^{M} f_{ik} w_k \right) \right) \right) \tag{15}$$

The final MPE algorithm is as follows:

1. Take as input a set of pixels from an HSI and a set of endmembers

2. Use quadratic programming to estimate the microscopic mixture proportions (f_{ik}'s) by minimizing the RSS in Equation (14)

3. Use quadratic programming to estimate the macroscopic mixture proportions (p_{ik}'s) by minimizing the RSS in Equation (15)

The resulting proportions are interpreted as follows. The macroscopic proportions *1* through *M* ($p_{i1} \cdots p_{iM}$) represent the proportions of endmembers macroscopically mixed. The *M+1* macroscopic proportion (p_{iM+1}) is the estimated proportion of the pixel composed of a microscopic mixture. Therefore, $p_{iM+1} f_{ik}$ is the proportion of the pixel described by a microscopic mixture of the kth endmember.

Returning to the diagram in Figure 2, the estimated microscopic mixture proportions result in a point r on the arc A that is the closest to the MMP mixture point. The estimated macroscopic mixture proportions find a minimal RSS solution within the simplex formed by the endmembers and the previously estimated point r. Typically, a unique estimation of the microscopic mixture proportions is not possible with the information contained within a given HSI pixel. Therefore, it is probable that some amount of estimation error will be introduced into the microscopic proportion estimation. This introduced error is due to the ill-posed inversion and is unavoidable in estimating proportions in the MMP model using only HSI spectral information.
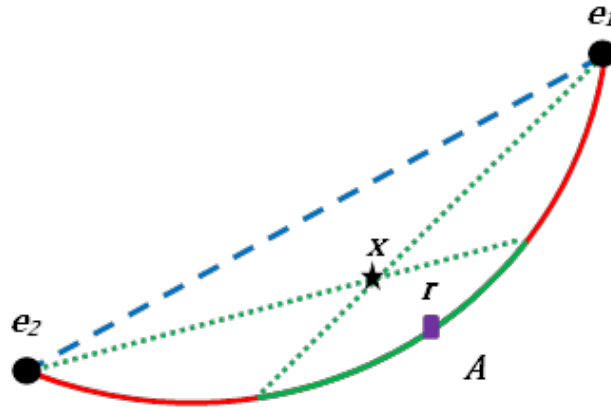
Figure 2: Diagram of multi-mixture pixel (black star) contained within the region bounded by the possible macroscopic mixtures (dashed blue line) and the possible microscopic mixtures (solid red curve) with plausible constituent microscopic mixture point (purple square).
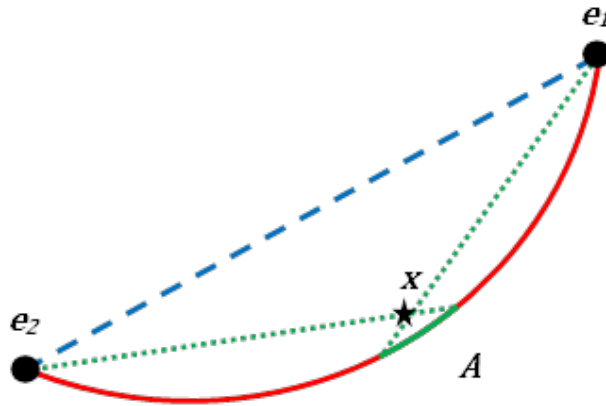

Figure 3: Diagram of multi-mixture pixel x contained within the region bounded by the possible macroscopic mixtures (dashed blue line) and the possible microscopic mixtures (solid red curve) with plausible constituent microscopic mixtures (green arc).
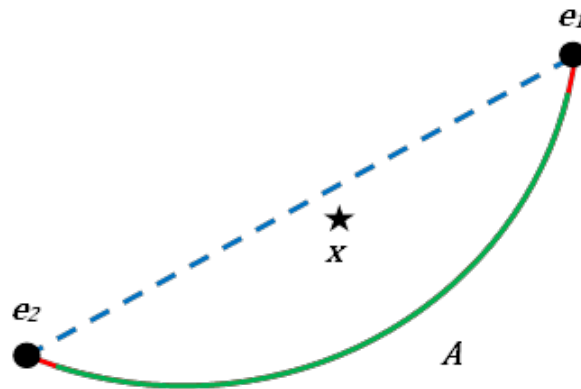

Figure 4: Diagram of multi-mixture pixel x contained within the region bounded by the possible macroscopic mixtures (dashed blue line) and the possible microscopic mixtures (solid red curve) with plausible constituent microscopic mixtures (green arc).

4. MMP ENDMEMBER EXTRACTION

The MMP model, shown in Equation (12), is composed of K endmembers, represented as e_k, and their respective albedo-domain signatures, represented by w_k where $w_k = R^{-1}(e_k)$. The MMP endmember extraction (MEE) algorithm uses an alternating optimization technique to minimize the regularized RSS shown in Equation (16), where the RSS term is given by Equation (15). The sum of squared differences (SSD) term, shown in Equation (17), keeps the endmembers

close to the data and the μ controls the tradeoff between error and regularization. This approach is derived from the Iterative Constrained Endmembers (ICE) algorithm.[1]

$$RSS_{reg} = (1 - \mu)\frac{RSS}{N} + \mu\frac{SSD}{M(M-1)} \tag{16}$$

$$SSD = \sum_{k=1}^{M-1} \sum_{l=k+1}^{M} (e_k - e_l)^t(e_k - e_l) \tag{17}$$

The algorithm alternates between estimating the proportions, using MPE, and the endmembers using Newton's method (Equation (18)). The derivative of RSS_{reg} for the jth endmember is shown in Equation (19), where $E = [e_1 | \cdots | e_M]$ and $= [w_1 | \cdots | w_M] = [R^{-1}(e_1) | \cdots | R^{-1}(e_M)]$. In this formulation u_i is the derivative of the reflectance function (Equation (7)) at the albedo-domain microscopic mixture (i.e., $u_i = \frac{\partial R}{\partial w_\lambda}(Wf_i)$) and v_j is the slope of the inverse reflectance function of the jth endmember. The second derivative of RSS_{reg} is given by Equation (20).

$$e_j^{new} = e_j^{old} - \eta \left(\frac{\frac{\partial RSS_{reg}}{\partial e_j}}{\frac{\partial^2 RSS_{reg}}{\partial e_j^2}} \right) \tag{18}$$

$$
\frac{\partial RSS_{reg}}{\partial e_j} = -2\frac{1-\mu}{N}\sum_{i=1}^{N} \left((p_{ij} + p_{iM+1}f_{ij}\odot v_j\odot u_i)\left(x_i - E^{old}p_i - p_{iM+1}R(Wf) \right) \right) \\
+ \frac{2\mu}{M(M-1)}\sum_{k=1;k\neq j}^{M} \left(e_j^{old} - e_k \right) \tag{19}
$$

$$\frac{\partial^2 RSS_{reg}}{\partial e_j^2} = 2\frac{1-\mu}{N}\sum_{i=1}^{N}\left(p_{ij} + p_{iM+1}f_{ij}\odot v_j\odot u_i \right)^2 + \frac{2\mu}{M} \tag{20}$$

The complete MEE algorithm is as follows:
1. Initialize by selecting a starting set of HSI pixels as the endmembers
2. Use the MPE algorithm to estimate the proportions of each pixel with the current endmembers
3. Use Newton's method to update the endmembers
4. Repeat steps 1 – 3 until a stopping criteria is met

5. EXPERIMENTAL RESULTS

A quantitative evaluation of the MEE algorithm was conducted using synthetic data and RELAB measurements of well-known mineral mixtures. Mean absolute band error (MABE), given by Equation (21), was used to quantify error between true (e_{dk}) and estimated ($\hat{e}_{dk}$) endmembers.

$$MABE = \frac{1}{N \cdot D}\sum_{d=1}^{D}\sum_{k=1}^{M}|e_{dk} - \hat{e}_{dk}| \tag{21}$$

5.1 Synthetic Data Sets Results

Synthetic data sets were created using the MMP model and three 38-dimensional endmembers obtained from the ASTER spectral library with proportions sampled from a Dirichlet distribution with additive zero-mean Gaussian noise.[89] Each data set consisted of 1,000 data points. A sample synthetic data set is shown in Figure 5 and Figure 6.
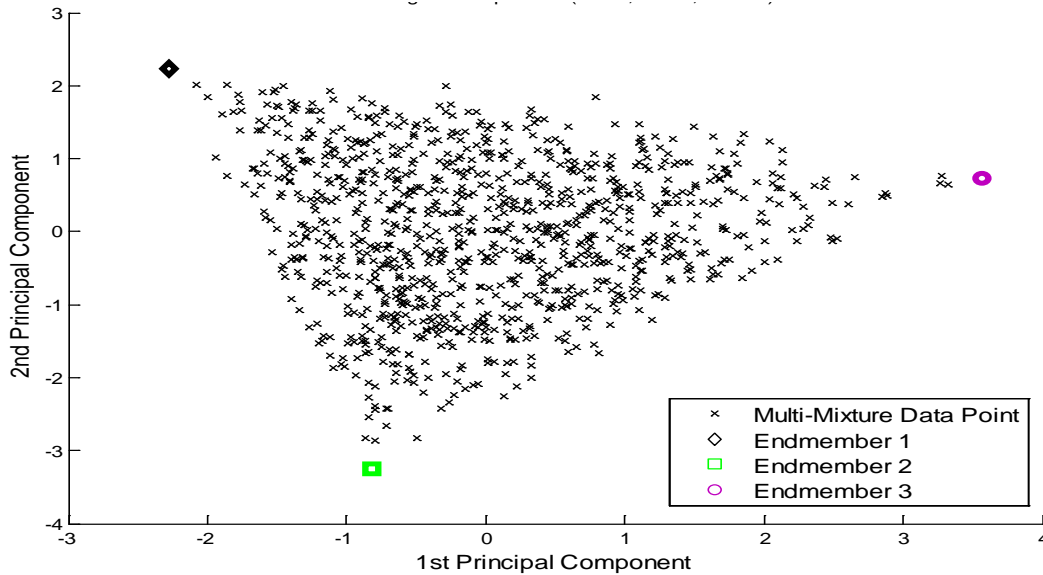
Figure 5: First and second principal components of a synthetic MMP data set created using three endmembers and proportions drawn from a Dirichlet distribution.
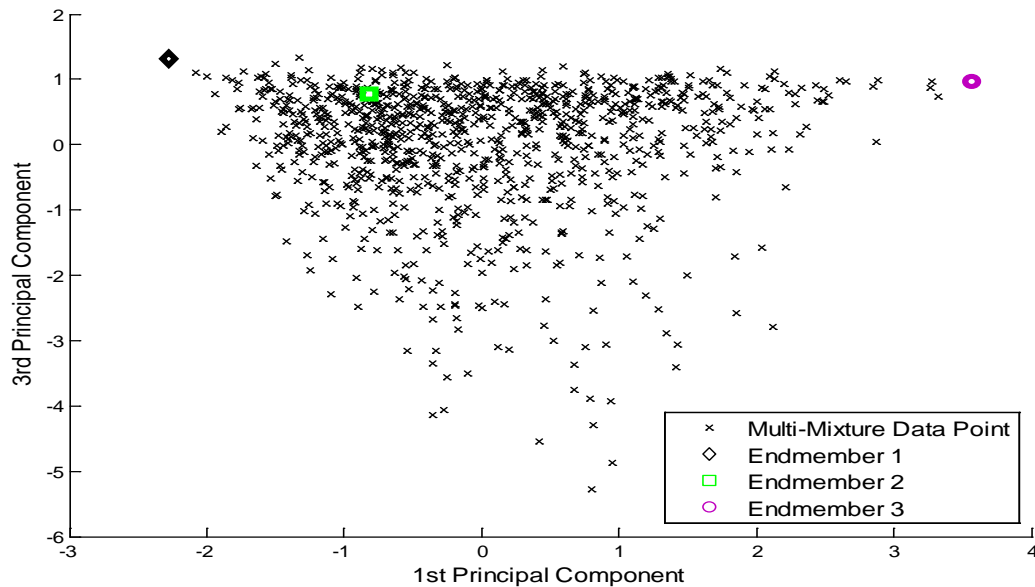

Figure 6: First and third principal components of a synthetic MMP data set created using three endmembers and proportions drawn from a Dirichlet distribution.

In these experiments 50 data sets were generated. For each of the 50 synthetic data sets six algorithms were run and the MABE calculated. The paired difference between MEE algorithm's MABE and the resulting MABE for the remaining algorithms was calculated. These results are shown in the histogram in Figure 7. The algorithms were MEE (shown in the figure's key as MMP), vertex component analysis (VCA)[12], ICE[1], regularized linear mixture model – gradient descent (RLMM-GD), albedo-domain RLMM-GD (AD-RLMM-GD), and macroscopic microscopic iterated constrained endmembers (MICE)[86]. RLMM-GD is a gradient descent solution to estimating the regularized RSS using the LMM. The RLMM-GD algorithm was used to make an algorithm as close to possible as MEE with the only exception being the linear only objective. The AD-RLMM-GD is similar to RLMM-GD except that the data points are converted to albedo-domain first and then solved with the LMM. The AD-RLMM-GD algorithm was used to ensure that the MEE algorithm is not solely benefiting from access to the albedo-domain form of the HSI pixels.
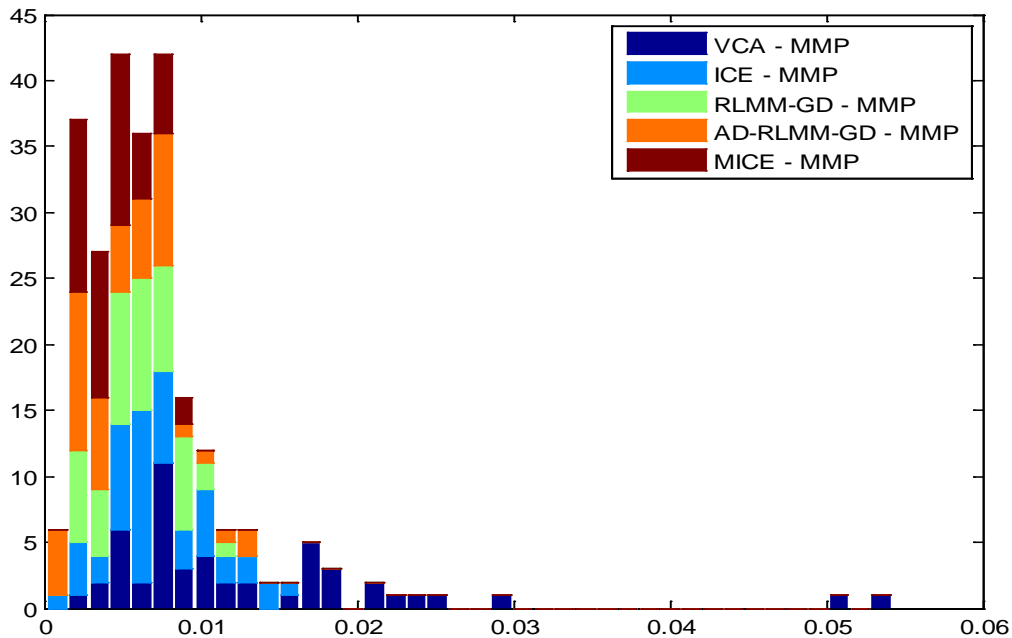
Figure 7: Histogram of paired MABE differences.

As can be seen from the histogram in Figure 7, in all cases the MEE algorithm created less error when estimating the endmembers of the synthetic data sets. VCA scored the worst, which is not surprising given its need for a pure-pixel assumption.[12] MICE scored best of the remaining algorithms, even though MEE still outperformed it. This result is also not surprising as MICE incorporates both macroscopic and microscopic mixtures but without the ability to model a multi-mixture pixel.[86]

5.2 RELAB Data Sets Results

The RELAB data sets used consist of mixtures of Enstatite with Olivine and Magnetite with Olivine. These mixtures where prepared and measured by Professors John Mustard and Carle Pieters of Brown University, as specified in their paper.[53] The spectra were collected with RELAB, a high-resolution bidirectional reflectance spectrometer with a specified angle of emergence of 0^0 and angle of incidence of 30^0.[53] Each mixture data set is composed of spectra from five mixed samples and two endmembers. The spectra have 211 dimensions with wavelengths ranging from 400 nm to 2,500 nm. These data sets have become a *de facto* standard for evaluating microscopic unmixing algorithms.[33, 38, 53, 59, 60]

The MABE resulting from the endmembers estimated with both MEE and ICE is shown in Figure 8. This histogram demonstrates that MEE is able to estimate the RELAB endmembers with less error than ICE. It should be noted that the RELAB data sets only contain five samples each.
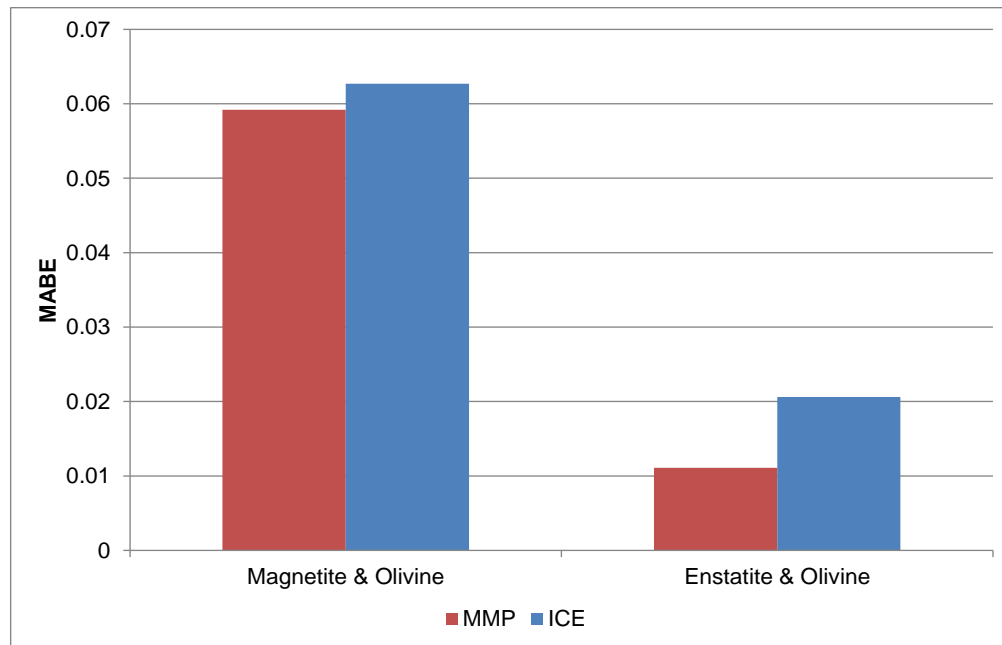
Figure 8: MABE histogram for RELAB data sets.

6. CONCLUSIONS AND FUTURE WORK

In this paper an algorithm, MEE, was presented to estimate endmembers of HSI pixels using the MMP model. Using synthetic data sets, it was demonstrated that pixels composed of multiple mixture types create increased error in estimating endmembers when using a linear model, or even the MICE algorithm. Through experimentation it was shown that MEE is able to accurately estimate the endmembers of data sets composed of multi-mixture pixels. Further analysis was done using the RELAB laboratory data sets of known microscopic mixtures. Using these data sets MEE was compared against a popular LMM endmember extraction algorithm, ICE.[1] Analysis revealed that MEE was able to accurately estimate the endmembers of the given RELAB data sets. Future research could investigate alternate ways of estimating the endmembers during the alternating optimization of the objective function. Also, future work could utilize LIDAR sensor data to increase the accuracy in estimating the angles of incidence and emergence used in the BRDF.

REFERENCES

[1]   Berman, M., Kiiveri, H., et al., "ICE: a statistical approach to identifying endmembers in hyperspectral images", Geoscience and Remote Sensing, IEEE Transactions on, 42(10), 2085-2095 (2004).
[2]   Dobigeon, N., Moussaoui, S., et al., "Bayesian separation of spectral sources under non-negativity and full additivity constraints", Signal Processing, 89(12), 2657-2669 (2009).
[3]   Eches, O., Dobigeon, N., et al., "An NCM-based Bayesian algorithm for hyperspectral unmixing", Hyperspectral Image and Signal Processing: Evolution in Remote Sensing, 2009. WHISPERS '09. First Workshop on, 1-4 (2009)
[4]   Nascimento, J. and Bioucas-Dias, J. M., "Learning dependent sources using mixtures of Dirichlet: Applications on hyperspectral unmixing", Hyperspectral Image and Signal Processing: Evolution in Remote Sensing, 2009. WHISPERS '09. First Workshop on, 1-5 (2009)
[5]   Zare, A., "Hyperspectral Endmember Detection and Band Selection Using Bayesian Methods", Computer & Information Science & Engineering, 136 (2008).
[6]   Zare, A. and Gader, P., "Sparsity Promoting Iterated Constrained Endmember Detection in Hyperspectral Imagery", Geoscience and Remote Sensing Letters, IEEE, 4(3), 446-450 (2007).
[7]   Zare, A. and Gader, P., "L1-Endmembers: A Robust Endmember Detection and Spectral Unmixing Algorithm", Proceedings of the SPIE Defense, Security, and Sensing, (2010).

[8]   Zare, A. and Gader, P. D., "Endmember detection using the Dirichlet process", Pattern Recognition, 2008. ICPR 2008. 19th International Conference on, 1-4 (2008)

[9]   Bioucas-Dias, J. M., "A variable splitting augmented Lagrangian approach to linear spectral unmixing", Hyperspectral Image and Signal Processing: Evolution in Remote Sensing, 2009. WHISPERS '09. First Workshop on, 1-4 (2009)

[10]   Boardman, J. W., "Automating spectral unmixing of AVIRIS data using convex geometry concepts", Summaries of the Fourth Annual JPL Airborne Geoscience Workshop, JPL Pub. 93-26, AVIRIS Workshop, 1(11-14 (1993).

[11]   Boardman, J. W., Kruse, F. A., et al., "Mapping Target Signatures Via Partial Unmixing of AVIRIS Data", Summaries, Fifth JPL Airborne Earth Science Workshop, JPL Publications, 1(23-26 (1995).

[12]   Nascimento, J. M. P. and Dias, J. M. B., "Vertex component analysis: a fast algorithm to unmix hyperspectral data", Geoscience and Remote Sensing, IEEE Transactions on, 43(4), 898-910 (2005).

[13]   Santos-Garcia, A. and Velez-Reyes, M., "Identifiability of geometric models for linear unmixing at different spatial resolutions in hyperspectral unmixing", Hyperspectral Image and Signal Processing: Evolution in Remote Sensing (WHISPERS), 2010 2nd Workshop on, 1-4 (2010)

[14]   Tsung-Han, C., Wing-Kin, M., et al., "Hyperspectral unmixing from a convex analysis and optimization perspective", Hyperspectral Image and Signal Processing: Evolution in Remote Sensing, 2009. WHISPERS '09. First Workshop on, 1-4 (2009)

[15]   Winter, M. E., "N-FINDR: An Algorithm for Fast Autonomous Spectral End-member Determination in Hyperspectral Data", SPIE Conference on Imaging Spectrometry V, 266-275 (1999)

[16]   Xiaoli, J., Yingzi, D., et al., "Component analysis-based unsupervised linear spectral mixture analysis for hyperspectral imagery", Hyperspectral Image and Signal Processing: Evolution in Remote Sensing, 2009. WHISPERS '09. First Workshop on, 1-5 (2009)

[17]   Keshava, N. and Mustard, J. F., "Spectral unmixing", Signal Processing Magazine, IEEE, 19(1), 44-57 (2002).

[18]   Villeneuve, P. V., Gerstl, S. A., et al., "Estimating nonlinear mixing effects for arid vegetation scenes with MISR channels and observation directions", Geoscience and Remote Sensing Symposium Proceedings, 1998. IGARSS '98. 1998 IEEE International, 1234-1236 vol.3 (1998)

[19]   Han, T. and Goodenough, D. G., "Investigation of Nonlinearity in Hyperspectral Imagery Using Surrogate Data Methods", Geoscience and Remote Sensing, IEEE Transactions on, 46(10), 2840-2847 (2008).

[20]   Ainsworth, T. L., Bachmann, C. M., et al., "Local intrinsic dimensionality of hyperspectral imagery from non-linear manifold coordinates", Geoscience and Remote Sensing Symposium, 2007. IGARSS 2007. IEEE International, 1541-1542 (2007)

[21]   Bachmann, C. M., Ainsworth, T. L., et al., "Improvements to land-cover and invasive species mapping from hyperspectral imagery in the Virginia Coast reserve", Geoscience and Remote Sensing Symposium, 2004. IGARSS '04. Proceedings. 2004 IEEE International, 4180-4183 vol.6 (2004)

[22]   Bachmann, C. M., Ainsworth, T. L., et al., "Exploiting manifold geometry in hyperspectral imagery", Geoscience and Remote Sensing, IEEE Transactions on, 43(3), 441-454 (2005).

[23]   Bachmann, C. M., Ainsworth, T. L., et al., "Improved Manifold Coordinate Representations of Large-Scale Hyperspectral Scenes", Geoscience and Remote Sensing, IEEE Transactions on, 44(10), 2786-2803 (2006).

[24]   Bachmann, C. M., Ainsworth, T. L., et al., "Automated Estimation of Spectral Neighborhood Size in Manifold Coordinate Representations of Hyperspectral Imagery: Implications for Anomaly Finding, Bathymetry Retrieval, and Land Applications", Geoscience and Remote Sensing Symposium, 2008. IGARSS 2008. IEEE International, I-56-I-57 (2008)

[25]   Bachmann, C. M., Ainsworth, T. L., et al., "Bathymetric Retrieval From Hyperspectral Imagery Using Manifold Coordinate Representations", Geoscience and Remote Sensing, IEEE Transactions on, 47(3), 884-897 (2009).

[26]   Bachmann, C. M., Ainsworth, T. L., et al., "Manifold coordinate representations of hyperspectral imagery: Improvements in algorithm performance and computational efficiency", Geoscience and Remote Sensing Symposium (IGARSS), 2010 IEEE International, 4244-4247 (2010)

[27]   Bachmann, C. M., Ainsworth, T. L., et al., "A new data-driven approach to modeling coastal bathymetry from hyperspectral imagery using manifold coordinates", OCEANS, 2005. Proceedings of MTS/IEEE, 2242-2249 Vol. 3 (2005)

[28]   Bachmann, C. M., Ainsworth, T. L., et al., "Modeling Coastal Waters from Hyperspectral Imagery using Manifold Coordinates", Geoscience and Remote Sensing Symposium, 2006. IGARSS 2006. IEEE International Conference on, 356-359 (2006)

[29]   Baoxin, H., Miller, J. R., et al., "Investigation of linear spectral mixtures of the reflectance spectra using laboratory simulated forest scenes", Geoscience and Remote Sensing Symposium, 2002. IGARSS '02. 2002 IEEE International, 1535-1537 vol.3 (2002)

[30]   Borel, C. C. and Gerstl, S. A. W., "Nonlinear spectral mixing models for vegetative and soil surfaces", Remote Sensing of Environment, 47(3), 403-416 (1994).

[31]   Chen, X. and Vierling, L., "Spectral mixture analyses of hyperspectral data acquired using a tethered balloon", Remote Sensing of Environment, 103(3), 338-350 (2006).

[32]   Fan, W., Hu, B., et al., "Comparative Study Between a New Nonlinear Model and Common Linear Model for Analysing Laboratory Simulated-Forest Hyperspectral Data", International Journal of Remote Sensing, 30(11), 2951-2962 (2009).

[33]   Guilfoyle, K. J., Althouse, M. L., et al., "A quantitative and comparative analysis of linear and nonlinear spectral mixture models using radial basis function neural networks", Geoscience and Remote Sensing, IEEE Transactions on, 39(10), 2314-2318 (2001).

[34]   Halimi, A., Altmann, Y., et al., "Nonlinear Unmixing of Hyperspectral Images Using a Generalized Bilinear Model", Geoscience and Remote Sensing, IEEE Transactions on, PP(99), 1-10 (2011).

[35]   Heylen, R., Burazerovic, D., et al., "A graph-based method for non-linear unmixing of hyperspectral imagery", Geoscience and Remote Sensing Symposium (IGARSS), 2010 IEEE International, 197-200 (2010)

[36]   Heylen, R. and Scheunders, P., "Nonlinear barycentric dimensionality reduction", Image Processing (ICIP), 2010 17th IEEE International Conference on, 1341-1344 (2010)

[37]   Licciardi, G. A., "Neural Network Algorithms for Nonlinear Spectral Unmixing Applied on Hyperspectral Data", Hyperspectral 2010 Workshop, (2010).

[38]   Plaza, J., Martinez, P., et al., "Nonlinear Neural Network Mixture Models for Fractional Abundance Estimation in AVIRIS Hyperspectral Images", NASA Jet Propulsion Laboratory AVIRIS Airborne Earth Science Workshop, (2004).

[39]   Plaza, J., Plaza, A., et al., "Joint linear/nonlinear spectral unmixing of hyperspectral image data", Geoscience and Remote Sensing Symposium, 2007. IGARSS 2007. IEEE International, 4037-4040 (2007)

[40]   Poulet, F. and Erard, S., "Nonlinear spectral mixing: Quantitative analysis of laboratory mineral mixtures", J. Geophys. Res., 109(E2), E02009 (2004).

[41]   Rahman, M. T. and Alam, M. S., "Nonlinear Unmixing of Hyperspectral Data Using BDRF and Maximum Likelihood Algorithm", SPIE Automatic Target Recognition XVII, (2007)

[42]   Raksuntorn, N. and Qian, D., "Nonlinear mixture analysis for hyperspectral imagery", Geoscience and Remote Sensing Symposium,2009 IEEE International,IGARSS 2009, III-829-III-832 (2009)

[43]   Raksuntorn, N. and Qian, D., "Nonlinear Spectral Mixture Analysis for Hyperspectral Imagery in an Unknown Environment", Geoscience and Remote Sensing Letters, IEEE, 7(4), 836-840 (2010).

[44]   Ray, T. W. and Murray, B. C., "Nonlinear spectral mixing in desert vegetation", Remote Sensing of Environment, 55(1), 59-64 (1996).

[45]   Somers, B., Cools, K., et al., "Nonlinear Hyperspectral Mixture Analysis for tree cover estimates in orchards", Remote Sensing of Environment, 113(6), 1183-1193 (2009).

[46]   Wang, X. R., Kumar, S., et al., "Probabilistic Classification of Hyperspectral Images by Learning Nonlinear Dimensionality Reduction Mapping", Information Fusion, 2006 9th International Conference on, 1-8 (2006)

[47]   Weiwei, S. and Chun, L., "Manifold Coordinates Repairing of Boundary Points with PLS for Isomap Nonlinear Dimensionality Reduction of Hyperspectral Image", Multi-Platform/Multi-Sensor Remote Sensing and Mapping (M2RSM), 2011 International Workshop on, 1-6 (2011)

[48]   Wonkook, K., Yangchi, C., et al., "Multiresolution manifold learning for classification of hyperspectral data", Geoscience and Remote Sensing Symposium, 2007. IGARSS 2007. IEEE International, 3785-3788 (2007)

[49]   Wu, B., Zhang, L., et al., "Nonlinear Estimation of Hyperspectral Mixture Pixel Proportion Based on Kernel Orthogonal Subspace Projection", Advances in Neural Networks - ISNN 2006, 1070-1075 (2006).

[50]   Xuehong, C., Jin, C., et al., "Impact of collinearity on linear and nonlinear spectral mixture analysis", Hyperspectral Image and Signal Processing: Evolution in Remote Sensing (WHISPERS), 2010 2nd Workshop on, 1-4 (2010)

[51]   Yangchi, C., Crawford, M. M., et al., "Applying nonlinear manifold learning to hyperspectral data for land cover classification", Geoscience and Remote Sensing Symposium, 2005. IGARSS '05. Proceedings. 2005 IEEE International, 4311-4314 (2005)

[52]   Yangchi, C., Crawford, M. M., et al., "Improved Nonlinear Manifold Learning for Land Cover Classification via Intelligent Landmark Selection", Geoscience and Remote Sensing Symposium, 2006. IGARSS 2006. IEEE International Conference on, 545-548 (2006)

[53]   Mustard, J. F. and Pieters, C. M., "Quantitative Abundance Estimates From Bidirectional Reflectance Measurements", Journal of Geophysical Research, 92(B4), E617-E626 (1987).

[54]   Mustard, J. F. and Pieters, C. M., "Photometric Phase Functions of Common Geologic Minerals and Applications to Quantitative Analysis of Mineral Mixture Reflectance Spectra", Journal of Geophysical Research, 94(B10), 13619-13634 (1989).

[55]   Hapke, B. and Wells, E., "Bidirectional Reflectance Spectroscopy 2. Experiments and Observations", Journal of Geophysical Research, 86(B4), 3055-3060 (1981).

[56]   Hapke, B., [Theory of Reflectance and Emittance Spectroscopy], Cambridge University Press, (1993).

[57]   Nash, D. B. and Conel, J. E., "Spectral Reflectance Systematics for Mixtures of Powdered Hypersthene, Labradorite, and Ilmenite", Journal of Geophysical Research, 79(11), 1615-1621 (1974).

[58]   Singer, R. B. and McCord, T. B., "Mars: Large scale mixing of bright and dark surface materials and implications for analysis of spectral reflectance", Proc. Lunar Planet. Sci. Conf. 10th, 1835-1848 (1979).

[59]   Broadwater, J. and Banerjee, A., "A generalized kernel for areal and intimate mixtures", Hyperspectral Image and Signal Processing: Evolution in Remote Sensing (WHISPERS), 2010 2nd Workshop on, 1-4 (2010)

[60]   Broadwater, J. and Banerjee, A., "A comparison of kernel functions for intimate mixture models", Hyperspectral Image and Signal Processing: Evolution in Remote Sensing, 2009. WHISPERS '09. First Workshop on, 1-4 (2009)

[61]   Hapke, B., "Bidirectional Reflectance Spectroscopy 1. Theory", Journal of Geophysical Research, 86(B4), 3039-3054 (1981).

[62]   Shkuratov, Y., Starukhina, L., et al., "A Model of Spectral Albedo of Particulate Surfaces: Implications for Optical Properties of the Moon", Icarus, 137(2), 235-246 (1999).

[63]   Broadwater, J. and Banerjee, A., "Mapping Intimate Mixtures Using An Adaptive Kernel-Based Technique", Workshop on Hyperspectral Image and Signal Processing: Evolution in Remote Sensing, (2011).

[64]   Banerjee, A., Burlina, P., et al., "A machine learning approach for finding hyperspectral endmembers", Geoscience and Remote Sensing Symposium, 2007. IGARSS 2007. IEEE International, 3817-3820 (2007)

[65]   Broadwater, J., Chellappa, R., et al., "Kernel fully constrained least squares abundance estimates", Geoscience and Remote Sensing Symposium, 2007. IGARSS 2007. IEEE International, 4041-4044 (2007)

[66]   Bachmann, C. M. and Ainsworth, T. L., "Bathymetric retrieval from manifold coordinate representations of hyperspectral imagery", Geoscience and Remote Sensing Symposium, 2007. IGARSS 2007. IEEE International, 1548-1551 (2007)

[67]   Bachmann, C. M., Ainsworth, T. L., et al., "Improved manifold coordinate representations of hyperspectral imagery", Geoscience and Remote Sensing Symposium, 2005. IGARSS '05. Proceedings. 2005 IEEE International, 4307-4310 (2005)

[68]   Dong, G., Zhang, Y., et al., "Dimensionality Reduction of Hyperspectral Data Based on ISOMAP Algorithm", Electronic Measurement and Instruments, 2007. ICEMI '07. 8th International Conference on, 3-935-3-938 (2007)

[69]   Jinhuan, W., Zheng, T., et al., "Feature extraction of hyperspectral images based on preserving neighborhood discriminant embedding", Image Analysis and Signal Processing (IASP), 2010 International Conference on, 257-262 (2010)

[70]   Karantzalos, K., "Intrinsic dimensionality estimation and dimensionality reduction through scale space filtering", Digital Signal Processing, 2009 16th International Conference on, 1-6 (2009)

[71]   Kuybeda, O., Malah, D., et al., "Anomaly Preserving $\ell_{2,\infty}$-Optimal Dimensionality Reduction Over a Grassmann Manifold", Signal Processing, IEEE Transactions on, 58(2), 544-552 (2010).

[72]   Li, M., Crawford, M. M., et al., "Anomaly detection for hyperspectral images using local tangent space alignment", Geoscience and Remote Sensing Symposium (IGARSS), 2010 IEEE International, 824-827 (2010)

[73]   Ling, C., Rui, H., et al., "Graph-based semi-supervised weighted band selection for classification of hyperspectral data", Audio Language and Image Processing (ICALIP), 2010 International Conference on, 1123-1126 (2010)

[74]   Merenyi, E., Csatho, B., et al., "Knowledge discovery in urban environments from fused multi-dimensional imagery", Urban Remote Sensing Joint Event, 2007, 1-13 (2007)

[75] Velasco-Forero, S., Angulo, J., et al., "Morphological image distances for hyperspectral dimensionality exploration using Kernel-PCA and ISOMAP", Geoscience and Remote Sensing Symposium,2009 IEEE International,IGARSS 2009, III-109-III-112 (2009)

[76] Yuan, Z., Bo, W., et al., "Edge detection on hyperspectral imagery via Manifold techniques", Hyperspectral Image and Signal Processing: Evolution in Remote Sensing, 2009. WHISPERS '09. First Workshop on, 1-4 (2009)

[77] Li, M., Crawford, M. M., et al., "Local Manifold Learning-Based k-Nearest-Neighbor for Hyperspectral Image Classification", Geoscience and Remote Sensing, IEEE Transactions on, 48(11), 4099-4109 (2010).

[78] Wei, D. and Crawford, M. M., "Locally consistent graph regularization based active learning for hyperspectral image classification", Hyperspectral Image and Signal Processing: Evolution in Remote Sensing (WHISPERS), 2010 2nd Workshop on, 1-4 (2010)

[79] Wonkook, K. and Crawford, M., "A novel adaptive classification method for hyperspectral data using manifold regularization kernel machines", Hyperspectral Image and Signal Processing: Evolution in Remote Sensing, 2009. WHISPERS '09. First Workshop on, 1-4 (2009)

[80] Wonkook, K. and Crawford, M. M., "Adaptive Classification for Hyperspectral Image Data Using Manifold Regularization Kernel Machines", Geoscience and Remote Sensing, IEEE Transactions on, 48(11), 4110-4121 (2010).

[81] Wonkook, K., Crawford, M. M., et al., "Spatially Adapted Manifold Learning for Classification of Hyperspectral Imagery with Insufficient Labeled Data", Geoscience and Remote Sensing Symposium, 2008. IGARSS 2008. IEEE International, I-213-I-216 (2008)

[82] Heylen, R., Burazerovic, D., et al., "Non-linear Spectral Unmixing by Geodesic Simplex Volume Maximization", Selected Topics in Signal Processing, IEEE Journal of, PP(99), 1-1 (2010).

[83] Nascimento, J. M. P. and Bioucas-Dias, J. M., "Unmixing Hyperspectral Intimate Mixtures", SPIE Image and Signal Processing for Remote Sensing XVI, (2010)

[84] Johnson, P. E., Smith, M. O., et al., "Quantitative Analysis of Planetary Reflectance Spectra with Principal Components Analysis", Journal of Geophysical Research, 90(C805-C810 (1985).

[85] Smith, M. O., Johnson, P. E., et al., "Quantitative Determination of Mineral Types and Abundances from Reflectance Spectra Using Principal Components Analysis", Journal of Geophysical Research, 90(Supplement), C797-C804 (1985).

[86] Close, R., Gader, P., et al., "Hyperspectral Unmixing Using Macroscopic and Microscopic Mixture Models", IEEE Journal of Selected Topics in Applied Earth Observations and Remote Sensing [under review], (2012).

[87] Close, R., Gader, P., et al., "Using physics-based macroscopic and microscopic mixture models for hyperspectral pixel unmixing", Algorithms and Technologies for Multispectral, Hyperspectral, and Ultraspectral Imagery XVIII, SPIE Defense, Security, and Sensing, (2012)

[88] Manolakis, D., Marden, D., et al., "Hyperspectral Image Processing for Automatic Target Detection Applications", Lincoln Laboratory Journal, 14(1), 79-116 (2003).

[89] Haykin, S., [Neural Networks and Learning Machines], Pearson Education, Inc., (2009).